



# The motion of rigid particles in the Poiseuille flow of pseudoplastic fluids through straight rectangular microchannels

Di Li<sup>1</sup> · Xiangchun Xuan<sup>1</sup>

Received: 20 December 2018 / Accepted: 11 March 2019  
© Springer-Verlag GmbH Germany, part of Springer Nature 2019

## Abstract

There has been in the past decade a significantly growing interest in the use of flow-induced lift forces for a passive control of particle motion in microchannels. This nonlinear microfluidic technique can be implemented in both Newtonian and non-Newtonian fluids. The motions of rigid particles in confined flows of viscoelastic fluids with and without shear-thinning effects have each been well studied in the literature. However, a comprehensive understanding of particle motion in inelastic shear-thinning fluids is still lacking. We present herein a systematic experimental study of the motion of rigid particles in the Poiseuille flow of pseudoplastic xanthan gum (XG) solutions through straight rectangular microchannels. We find that the number and location of particle equilibrium positions are both a strong function of channel dimension, particle size and XG concentration. We attempt to explain the experimental observations using the competition of inertial and elastic lift forces acting on particles. Our experimental results imply a potentially high throughput separation of rigid particles by size in XG solutions.

**Keywords** Shear thinning · Particle motion · Elastic lift · Inertial lift · Non-Newtonian · Microfluidics

## 1 Introduction

Since the development of polydimethylsiloxane (PDMS)-based soft lithography technique (Duffy et al. 1998), microfluidic devices have been widely used to focus (Xuan et al. 2010), trap (Huang et al. 2017), concentrate (Nilsson et al. 2009), and separate (Sajeesh and Sen 2014) particles (from biological cells to synthetic beads, rigid particles to soft drops etc.) for many chemical, biomedical and environmental applications (Karimi et al. 2013; Novo et al. 2016; Sibbitts et al. 2018). A variety of external force fields (e.g., acoustic (Connacher et al. 2018), electric (Lapizco-Encinas 2018), magnetic (Munaz et al. 2018) and optical (Yang and Gijss 2018) fields) have thus far been demonstrated to *actively* control the motion of particles in these devices. However,

there has recently been a significantly growing interest in the use of flow-induced inherent lift and/or drag forces for a passive control of particle motion in microchannels (Amini et al. 2014; Liu and Hu 2017). This nonlinear microfluidic technique (Stoecklein and Di Carlo 2018) has been implemented in both Newtonian (Di Carlo 2009; Martel and Toner 2014; Zhang et al. 2016a) and non-Newtonian (D'Avino and Maffettone 2015; Lu et al. 2017; Yuan et al. 2018) fluids. It has the capability to achieve a very high throughput with the advantages of simplicity and effectiveness (Hur et al. 2010; Lim et al. 2014a). Moreover, it has the potential to integrate with an active particle manipulation technique [e.g., dielectrophoresis (Kung et al. 2016) or magnetophoresis (Del Giudice et al. 2015b; Kim et al. 2016; Zhang et al. 2016b; Zhou et al. 2017; and; Chen et al. 2017)] for enhanced sensitivity, specificity and flexibility (Yan et al. 2017).

The lift forces on particles in passive microfluidic techniques can be induced by three different effects: fluid inertia, fluid non-Newtonian rheology, and particle deformation (Leal 1980). The inertia of fluid causes rigid particles to move across the flow towards specific lateral positions in Newtonian fluids (Segre and Silberberg 1961; Ho and Leal 1974). Such an inertial focusing is the foundation of the so-called inertial microfluidics (Di Carlo 2009) that has found

---

This article is part of the topical collection “Particle motion in non-Newtonian microfluidics” guest edited by Xiangchun Xuan and Gaetano D’Avino.

---

✉ Xiangchun Xuan  
xcxuan@clemson.edu

<sup>1</sup> Department of Mechanical Engineering, Clemson University, Clemson, SC 29634-0921, USA

wide applications (Zhang et al. 2016a; Gou et al. 2018; Stoecklein and Di Carlo 2018) since its first demonstration in PDMS-based rectangular microchannels (Di Carlo et al. 2007). The non-Newtonian properties of fluid yield an elastic lift (Karnis et al. 1963; Karnis and Mason 1966) because of the gradients in normal stress differences, which directs particles towards the low shear rate regions in the absence of fluid inertia (Ho and Leal 1976; Leal 1979). The shape change causes deformable particles to move towards either the channel center or walls depending on the ratio of the dispersed-to-continuous fluid viscosity (Mortazavi and Tryggvason 2000; Takemura et al. 2009; Geislinger and Franke 2014).

The motion of rigid particles in the flow of non-Newtonian fluids through microchannels has been increasingly studied (D'Avino et al. 2017; Lu et al. 2017; Yuan et al. 2018) since the work of Leshansky et al. (2007). A range of viscoelastic polymer solutions [e.g., polyvinylpyrrolidone (PVP) (Romeo et al. 2013; Del Giudice et al. 2013; Xiang et al. 2016a, 2018), polyethylene oxide (PEO) (Lee et al. 2013; Li et al. 2016, 2018; Liu et al. 2015, 2017; Lu and Xuan 2015; Lu et al. 2015; Tian et al. 2018; Yuan et al. 2015, 2016; Xiang et al. 2016b), and polyacrylamide (PAA) (Leshansky et al. 2007; Lim et al. 2014b)] and biological fluids [e.g., hyaluronic acid (HA) (Lim et al. 2014a; Nam et al. 2015; Asghari et al. 2017) and DNA solutions (Kang et al. 2013; Kim and Kim 2016)] have been tested, where fluid elasticity and shear thinning are each found to play a significant role in the lateral particle migration. Specifically, the fluid elasticity effect causes particles to move to the region(s) of the lowest shear rate (Yang et al. 2012; Villone et al. 2013; Seo et al. 2014b), which is, however, strongly influenced by the fluid inertial effect (Yang et al. 2011; Villone et al. 2013; Li et al. 2015). The fluid shear-thinning effect promotes the particle migration away from the channel centerline (Huang and Joseph 2000; D'Avino et al. 2012; Seo et al. 2014a; Del Giudice et al. 2015a, 2017; Liu et al. 2016; Song et al. 2016).

In a recent study, we performed a systematic experimental study of both the individual and the combined effects of fluid inertia, elasticity and shear thinning on the motion of rigid spherical particles in a straight rectangular microchannel (Li and Xuan 2018). We tested the particle motion in four types of non-Newtonian fluids with distinct rheological properties: strongly elastic PVP solution with a negligible shear-thinning effect (Liu et al. 2015), inelastic xanthan gum (XG) solution with a strong shear-thinning effect (Japper-Jaafar et al. 2010), moderately elastic PEO solution with a relatively weak shear-thinning effect (Rodd et al. 2005; De Santo et al. 2014), and strongly elastic PAA solution with a strong shear-thinning effect (Poole and Escudier 2004). As noted above, the motions of rigid particles in confined flows of viscoelastic PVP, PEO and PAA solutions as well as

viscoelastic DNA and HA solutions with varying parameters have each been investigated in the literature (Liu and Hu 2017; Lu et al. 2017; Yuan et al. 2018). However, a comprehensive understanding of particle motion in inelastic shear-thinning [i.e., pseudoplastic (Gauthier et al. 1971a, b)] fluids is still lacking. We, therefore, perform in this work a detailed parametric study of the effects of channel dimension, particle size and polymer concentration on the motion of rigid particles in the Poiseuille flow of XG solutions through straight rectangular microchannels. We wish this work along with other recent papers as reviewed above would improve our understanding of how fluid rheological properties affect particle motion in microchannels.

## 2 Experiment

### 2.1 Particle suspensions

Three concentrations of XG solutions were used in our experiments: 500 ppm, 2000 ppm and 3750 ppm. They were each prepared by dissolving a certain amount of XG powders (Tokyo Chemical Industry) into deionized water (Fisher Scientific). XG solutions have been long known to be strongly shear thinning with little elasticity (Dhahir and Walters 1989; Lindner et al. 2000; Aytouna et al. 2013; Haase et al. 2017). The rheological properties of our prepared XG solutions are listed in Table 1, which are extracted from the literature (Japper-Jaafar et al. 2010) due to the lack of measuring equipment in our lab. Their viscosities,  $\eta$ , can be estimated using the Carreau-Yasuda model (Yasuda et al. 1981) based on the average fluid shear rate across the microchannel width,  $\bar{\gamma} = 2V/w$ ,

$$\frac{\eta - \eta_{\infty}}{\eta_0 - \eta_{\infty}} = \left[ 1 + (\lambda_{CY} \bar{\gamma})^a \right]^{(n-1)/a} \quad (1)$$

In the above,  $V$  is the average fluid velocity,  $w$  is the channel width,  $\eta_{\infty}$  is the infinite-shear-rate viscosity,  $\eta_0$  is the zero-shear-rate viscosity,  $\lambda_{CY}$  is a time constant,  $n$  is the power-law index, and  $a$  is a fitting parameter. The values of these parameters for the three types of XG solutions are

**Table 1** Rheological properties (refer to Eq. (1) for the definitions of symbols) of the prepared XG solutions at 20 °C

XG concentration (ppm)	$n$	$\eta_0$ (Pa s)	$\eta_{\infty}$ (Pa s)	$\lambda_{CY}$ (s)	$a$
500	0.58	$1.97 \times 10^{-2}$	$1.13 \times 10^{-3}$	$3.88 \times 10^{-1}$	2.10
2000	0.34	3.68	$2.24 \times 10^{-3}$	$2.15 \times 10^{+1}$	0.81
3750	0.19	$2.85 \times 10^{+2}$	$4.60 \times 10^{-3}$	$4.14 \times 10^{+2}$	1.47

All values are extracted from Japper-Jaafar et al. (2010)

given in Table 1. Spherical fluorescent (green) polystyrene particles of 10 μm in diameter (Thermo Scientific) were re-suspended in each of the prepared solutions for the study of XG concentration effect. Additionally, spherical fluorescent particles of 5 μm (Thermo Scientific) and 20 μm (Phosphorex) in diameter were re-suspended into 2000 ppm XG solution for the study of particle size effect.

### 2.2 Experimental setup

Figure 1a shows a picture of the straight rectangular microchannel, which was fabricated with polydimethylsiloxane (PDMS) using a custom-modified soft lithography technique as described elsewhere (Liang et al. 2011). The channel was measured 2 cm long with a fixed width of 68 (±2) μm. It was, however, made to have three different depths, i.e., 30 μm, 54 μm and 127 μm, for the study of channel aspect ratio effect on particle motion in XG solutions. At each end of the microchannel was there an expansion region with an array of patterned posts for the filtration of any debris. We used a right-angle prism (NT 32-526, Edmund Optics Inc.) to visualize the particle motion in the vertical plane of the microchannel (i.e., side view), which complemented the view in the horizontal plane (i.e., top view). The prism was pre-embedded into the PDMS slab and placed right before the outlet expansion with a 400 μm distance from the channel edge. The prepared particle suspension was driven through the microchannel using a syringe pump (KD Scientific). Particle motion was recorded through an

inverted fluorescent microscope (Nikon Eclipse TE2000U, Nikon Instrument) with a CCD camera (Nikon DS-Qi1Mc) at a rate of around 15 frame/s. Particle streak images were generated by stacking a sequence of snapshot images with the maximum intensity projection in Nikon imaging software (NIS-Elements AR 2.30). Particle intensity plots were obtained from reading the values of gray scale intensity of particle images in MATLAB®, which were then scaled (after the background intensity was subtracted) and plotted over the channel width or depth.

## 3 Theory

### 3.1 Force analysis

Figure 1b shows schematically the inertial and elastic lift forces acting on a neutrally buoyant spherical particle in the flow of XG solutions through a straight rectangular microchannel. The fluid inertia-driven lift,  $F_{iL}$ , can be broken into two competing components: the wall-induced inertial lift,  $F_{iL_w}$ , pushes the particle away from any channel walls because of the pressure increase in the particle–wall gap; the shear gradient-induced inertial lift,  $F_{iL_s}$ , directs the particle towards the high shear-rate region, i.e., the center of each face (see the contour of fluid shear rate in Fig. 1b), because of the curvature of fluid velocity profile (Ho and Leal 1974; Leal 1980; Di Carlo 2009). The following formula has been often suggested to evaluate the total inertial lift (Asmolov 1999),

$$F_{iL} = F_{iL_w} + F_{iL_s} \sim \rho d^4 \dot{\gamma}^2, \tag{2}$$

where  $\rho$  is the fluid density,  $d$  is the particle diameter, and  $\dot{\gamma}$  is the local fluid shear rate.

The fluid elasticity-driven lift,  $F_{eL}$ , results from the non-uniform normal stress differences in non-Newtonian fluid flows (Leal 1979; D’Avino et al. 2017). As the magnitude of second normal stress difference,  $N_2$ , is usually much smaller than that of the first normal stress difference,  $N_1$ , in polymer solutions (Bird et al. 1987),  $F_{eL}$  can be viewed proportional to the variation of  $N_1$  over the size of the particle (Leshansky et al. 2007), i.e.,

$$F_{eL} \sim d^3 \nabla N_1 \tag{3}$$

Similar to other diluted solutions of high molecular weight polymers (Barnes et al. 1989),  $N_1$  of XG solutions, though small, has been demonstrated (Escudier and Smith 1999; Won and Kim 2004) to exhibit a power-law behavior,  $N_1 = A \dot{\gamma}^m$ , where  $A$  and  $m$  are both fluid-dependent constants with  $m$  typically in the range  $1 < m \leq 2$  (Barnes et al. 1989). Hence, Eq. (3) can be rewritten as:

$$F_{eL} \sim d^3 A \nabla \dot{\gamma}^m, \tag{4}$$

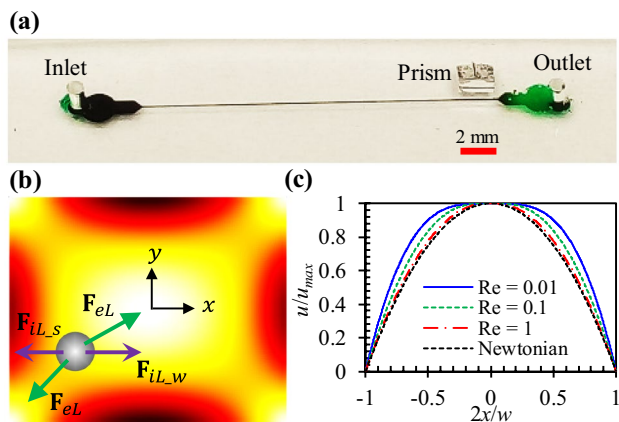


**Fig. 1** a Picture of a straight rectangular microchannel with a right-angle prism embedded before the outlet expansion for viewing the particle motion from the side; b schematic illustration of the inertial and elastic lift forces acting on a particle in the flow of XG solution through a straight rectangular microchannel, where the background color shows the contour of fluid shear rate,  $\dot{\gamma}$  (the darker the larger magnitude), in the cross-section; c widthwise profile of the flow velocity,  $u(x, y)$  (scaled by the maximum velocity,  $u_{max}$ ), for Newtonian ( $n = 1$ ) and shear-thinning ( $n = 0.3$ ) fluids at varying values of  $Re$  in a straight rectangular microchannel

where  $\mathbf{F}_{eL}$  points towards the low shear rate region, i.e., the center and four corners of the channel cross-section (see the shear rate contour in Fig. 1b).

Due to their strong dependences on the local shear rate,  $\dot{\gamma}$ , the inertial and elastic lift forces are both affected by the fluid velocity profile. As viewed from the plot in Fig. 1c, the velocity profile of a shear-thinning fluid flow ( $n = 0.3$  as an example) gets flat near the channel center in the absence of inertia, in contrast to the parabolic profile of a Newtonian fluid flow ( $n = 1$ ). Therefore, the shear gradient-induced inertial lift,  $\mathbf{F}_{iL_s}$ , may become different near the channel center in the flow of XG solutions. Such a variation should work with the additional elastic lift,  $\mathbf{F}_{eL}$ , to shift the equilibrium particle positions in XG solutions as compared to those in Newtonian fluids, which has been demonstrated in our recent study (Li and Xuan 2018). Specifically, we observed that 10  $\mu\text{m}$  particles migrate to both the channel center and corners (i.e., the lowest shear rate region, see the background color in Fig. 1b) in an inertia-less flow of 2000 ppm XG solution through a nearly square microchannel. Increasing the fluid inertia shifts particles away from both the center and corner equilibrium positions towards a mid-plane in between.

### 3.2 Dimensionless numbers

The inertial and elastic lift forces are both a strong function of the (channel) Reynolds number,

$$Re = \frac{\rho V D_h}{\eta(\bar{\dot{\gamma}})} = \frac{2\rho Q}{\eta(\bar{\dot{\gamma}})(w+h)}, \quad (5)$$

where  $D_h$  is the hydraulic diameter of the microchannel,  $\eta(\bar{\dot{\gamma}})$  is the fluid viscosity estimated via Eq. (1) using the average fluid shear rate across the channel width,  $Q$  is the volumetric flow rate, and  $h$  is the channel height. The value of  $Re$  is used to study the flow rate effect, and that of the power-law index,  $n$ , in Eq. (1) is used to study the XG concentration effect. The particle size effect is studied using the confinement ratio,

$$\beta = d/D_h, \quad (6)$$

and the channel dimension effect is studied using the aspect ratio,

$$AR = w/h. \quad (7)$$

Another dimensionless number that is often used to characterize the inertial lift is the particle Reynolds number (Di Carlo 2009),

$$Re_p = \beta^2 Re. \quad (8)$$

Note that  $Re_p > 0.1$  has been suggested as one criterion for effective inertial focusing of particles in straight

rectangular microchannels (Amini et al. 2014; Martel and Toner 2014).

## 4 Results and discussion

### 4.1 Effect of channel depth

Figure 2 illustrates the motions of 10  $\mu\text{m}$  particles in the flow of 2000 ppm XG solution through straight rectangular microchannels of 30  $\mu\text{m}$  ( $AR = 2.27$ ), 54  $\mu\text{m}$  ( $AR = 1.26$ ) and 127  $\mu\text{m}$  ( $AR = 0.54$ ) depths, respectively, within the same range of flow rates. In a roughly square microchannel with  $AR = 1.26$ , particles are seen from the top- and side-view images in Fig. 2b to travel near the channel center and corners when the flow rate is no higher than 1 mL/h (at which  $Re = 0.78$ ). This migration is primarily a result of the elastic lift,  $\mathbf{F}_{eL}$ , which, in the absence of inertial focusing (because of  $Re_p < 0.02$ ) (Di Carlo 2009), should direct particles towards the low shear rate regions over the channel cross-section (see the contour of fluid shear rate in the right-most schematic of Fig. 2b). Increasing the flow rate leads to an enhanced inertial lift, which, as reported in our previous study (Li and Xuan 2018), acts to push particles away from both the channel center (due to the shear gradient-induced inertial lift component,  $\mathbf{F}_{iL_s}$ ; see Fig. 1b) and corners (due to the wall-induced inertial lift component,  $\mathbf{F}_{iL_w}$ ; see Fig. 1b) towards a mid-plane in between. It also enhances the elastic lift though at a smaller rate as viewed from the dissimilar shear rate dependences of the two lift forces in Eq. (2) and Eq. (4), respectively. It is important to note that the velocity profile of shear-thinning fluids becomes closer to that of Newtonian fluids with the increase of flow rate as demonstrated in Fig. 1c. Therefore,  $\mathbf{F}_{iL_s}$  though vanishingly small near the channel centerline at a small  $Re$  because of the locally zero-shear rate, grows with increasing  $Re$ . The elasto-inertial equilibrium positions at the flow rate of 10 mL/h are schematically shown in the cross-sectional view of Fig. 2b.

In a shallower microchannel with a larger  $AR = 2.27$  (Fig. 2a), the inertial effect starts altering the elastic equilibrium positions near the channel center and corners at the flow rate of 1 mL/h (at which  $Re = 1.39$ ) because of the increase in both  $Re$  and particle confinement ratio ( $\beta = 0.24$ ) as compared to the roughly square microchannel (where  $Re = 0.78$  and  $\beta = 0.17$ ) in Fig. 2b. This phenomenon takes place even earlier (at 0.4 mL/h in Fig. 2a) in the vertical plane of the microchannel, where the elastic and inertial lift forces both increase due to the greater shear rate and shear rate gradients therein. The equilibrium particle positions at higher flow rates turn out to be similar to those in the microchannel with  $AR = 1.26$  in Fig. 2b, except that the elasto-inertial particle focusing in the former is visually better (particularly in the depth direction, see the images at



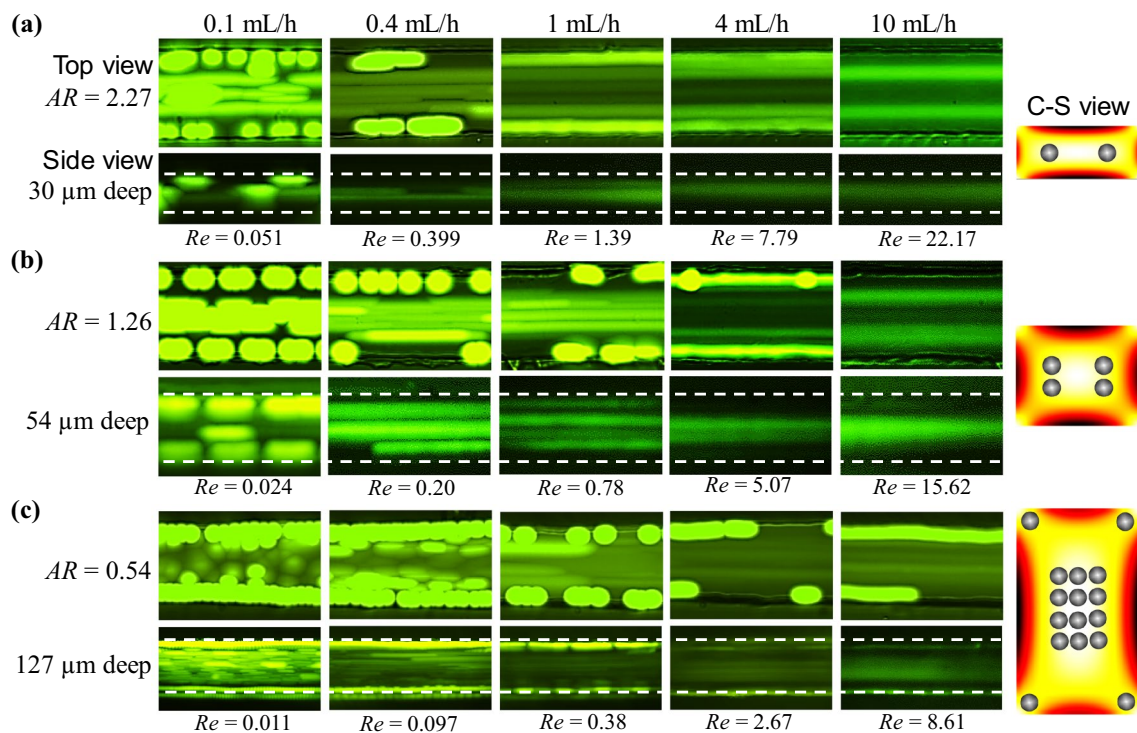


**Fig. 2** Migration of 10  $\mu\text{m}$  particles in the flow of 2000 ppm XG solution through straight rectangular microchannels of varying depths: **a** 30  $\mu\text{m}$  deep (with an aspect ratio of  $AR = 2.27$ ); **b** 54  $\mu\text{m}$  deep ( $AR = 1.26$ ); **c** 127  $\mu\text{m}$  deep ( $AR = 0.54$ ). The volumetric flow rate increases from 0.1 mL/h to 10 mL/h and the corresponding values of  $Re$  are highlighted below the images. The particle images in the upper and lower rows of (**a–c**) represent the top and side views,

respectively, at the channel outlet. The schematics in the right-most column illustrate the equilibrium particle positions over the cross-section (C-S) of each microchannel (estimated from the top and side view images at 10 mL/h, drawn to scale), where the background color shows the contour of fluid shear rate (the darker the larger magnitude) in the XG solution

10 mL/h in Fig. 2a) due to the greater particle confinement therein. In the deepest microchannel with  $AR = 0.54$ , particles are not observed from the images in Fig. 2c to move away from the channel center or corners in the entire range of flow rates under test. Moreover, those particles traveling around the channel center do not exhibit an apparent focusing trend like that in the two shallower microchannels (Fig. 2a, b). Three factors could possibly play a role in these observations. Firstly, the fluid inertia is the weakest in the deepest channel at the same flow rate, which reduces both the elastic and inertial lift forces. Secondly, the low shear rate region significantly expands as compared to the shallower microchannels, especially at the channel corners (see the contour of fluid shear rate in the right-most schematic of Fig. 2c), which increases the elastic force towards the corners while decreasing that towards the channel center. Thirdly, the particle confinement ratio becomes the smallest ( $\beta = 0.11$ ) among the three microchannels, which should also weaken both of the flow-induced lift forces.

The above trends for particle motion in XG solutions through microchannels of varying depths are quantitatively illustrated by the plots of particle intensity in Fig. 3. The

intensity values were obtained directly from the particle images in Fig. 2, and further scaled to different levels for distinguishing the curves at different flow rates (specifically, 0.8, 0.5, and 0.2 for 0.1 mL/h, 1 mL/h and 10 mL/h, respectively). It is seen from the intensity curves in the horizontal plane (Fig. 3a) that particles are overall pushed away from the walls when the channel depth decreases or the flow rate increases. Two primary particle positions, which should be (approximately) symmetric with respect to the channel center, are observed in each depth of microchannel. Their separation distance, however, appears to become smaller in a shallower channel. The intensity curves in the vertical plane (Fig. 3b) demonstrate a similar trend to that in the horizontal plane. However, the number of equilibrium particle positions reduces to one at the channel center in the two shallower microchannels if the flow rate is sufficiently high.

## 4.2 Effect of particle size

Figure 4 compares the motions of 5  $\mu\text{m}$ , 10  $\mu\text{m}$  and 20  $\mu\text{m}$  particles in the flow of 2000 ppm XG solution through a 54  $\mu\text{m}$  deep rectangular channel ( $AR = 1.26$ ) in the same

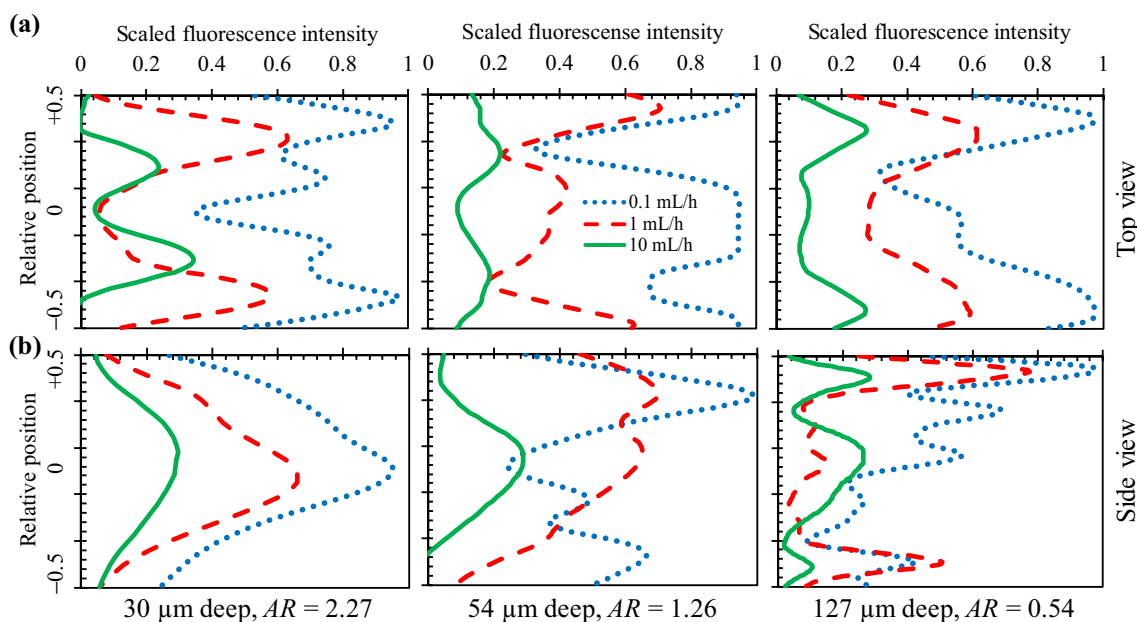


**Fig. 3** Scaled intensity plots for 10  $\mu\text{m}$  particles in the flow of 2000 ppm XG solution through microchannels of 30  $\mu\text{m}$ , 54  $\mu\text{m}$  and 127  $\mu\text{m}$  depths at the flow rates of 0.1 mL/h, 1 mL/h and 10 mL/h,

respectively: **a** in the horizontal plane of the channel; **b** in the vertical plane of the channel. The intensity values in **a** and **b** were obtained from the top- and side-view particle images, respectively, in Fig. 2

range of flow rates. When the flow rate is not higher than 1 mL/h (at which  $Re = 0.78$  and hence inertial effects are still insignificant), both 5  $\mu\text{m}$  (Fig. 4a) and 20  $\mu\text{m}$  (Fig. 4c) particles behave similar to 10  $\mu\text{m}$  ones (Fig. 4b). They all travel near the channel center and corners in the top-view images at the channel outlet because of the primary action of the elastic lift. With the further increase of flow rate, inertial lift starts playing a role in the motion of each type of particles. However, as the elastic lift in Eq. (4) is a weaker

function of particle size than the inertial lift in Eq. (2), their relative magnitude (i.e., elastic to inertial ratio) increases for smaller particles. Therefore, the elastic effect should remain dominant for 5  $\mu\text{m}$  particles at increasing flow rates, which explains why their motion does not change strongly with flow rate in Fig. 4a. Moreover, similar to 10  $\mu\text{m}$  particles in the 127  $\mu\text{m}$  deep microchannel (Fig. 2c), those 5  $\mu\text{m}$  particles that travel around the channel center do not achieve a noticeable focusing because of the small confinement ratio,

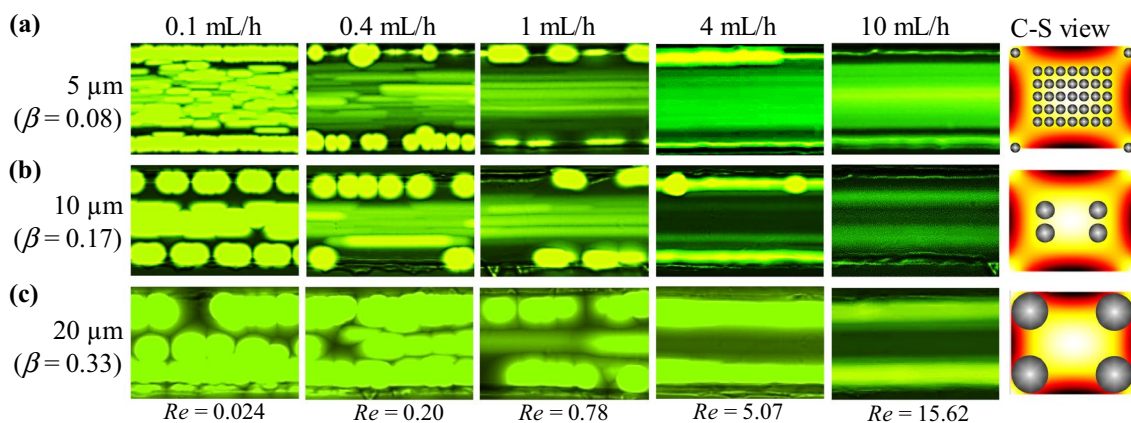


**Fig. 4** Migration of 5  $\mu\text{m}$  (with a confinement ratio of  $\beta = 0.08$ , **a**), 10  $\mu\text{m}$  ( $\beta = 0.17$ , **b**) and 20  $\mu\text{m}$  ( $\beta = 0.33$ , **c**) particles in the flow of 2000 ppm XG solution through a 54  $\mu\text{m}$  deep straight rectangular microchannel under varying flow rates. The corresponding values of  $Re$  (independent of particle size) are highlighted below the particle

images (top view) at the channel outlet. The schematics in the right-most column illustrate the equilibrium particle positions over the channel cross-section (C-S) (estimated from the images at 10 mL/h, drawn to scale), where the background color shows the contour of fluid shear rate (the darker the larger magnitude) in the XG solution

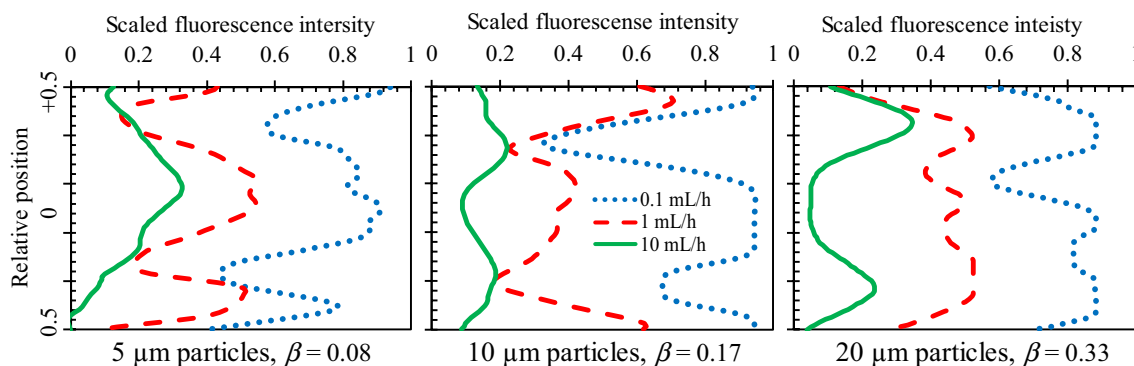
$\beta = 0.08$  (see the schematic in Fig. 4a, where the particles and channel are drawn to scale). We did not test even smaller particles than  $5 \mu\text{m}$ , but estimated the smallest manipulatable particles in XG solutions may be comparable to those in Newtonian fluids, i.e., with a confinement ratio of the order of 0.1 (Di Carlo 2009; Martel and Toner 2014; Zhang et al. 2016a).

In contrast, as the inertial effect increases faster than the elastic lift for larger particles,  $20 \mu\text{m}$  particles are observed from the top-view images in Fig. 4c to move away from the channel center at the flow rate of  $4 \text{ mL/h}$  and above. However, they are not directed towards a mid-plane in between the channel center and corners like  $10 \mu\text{m}$  particles (Fig. 4b). Instead,  $20 \mu\text{m}$  particles sustain the near-corner equilibrium positions in the range of flow rates under test, which seems to resemble the near-wall (more specifically, near the center of each face) motion of large particles in confined inertial flows (Di Carlo et al. 2009) because of the fairly large confinement ratio,  $\beta = 0.33$  (see the schematic in Fig. 4c). It is important to note from Fig. 4b,c that we may separate  $20 \mu\text{m}$  and  $10 \mu\text{m}$  particles via the differential elasto-inertial focusing in 2000 ppm XG solution. The motions of the three types of particles in Fig. 4 are also quantitatively demonstrated using the scaled particle intensity plots in Fig. 5. With the decrease of particle size, the primary elasto-inertial equilibrium positions in the horizontal plane shift from two near the corners to one along the channel center. Moreover, particles of any sizes are overall pushed away from the channel walls when the flow rate increases, which is similar to that of  $10 \mu\text{m}$  particles in microchannels of different depths (see Fig. 3) because of the increasing inertial effect.

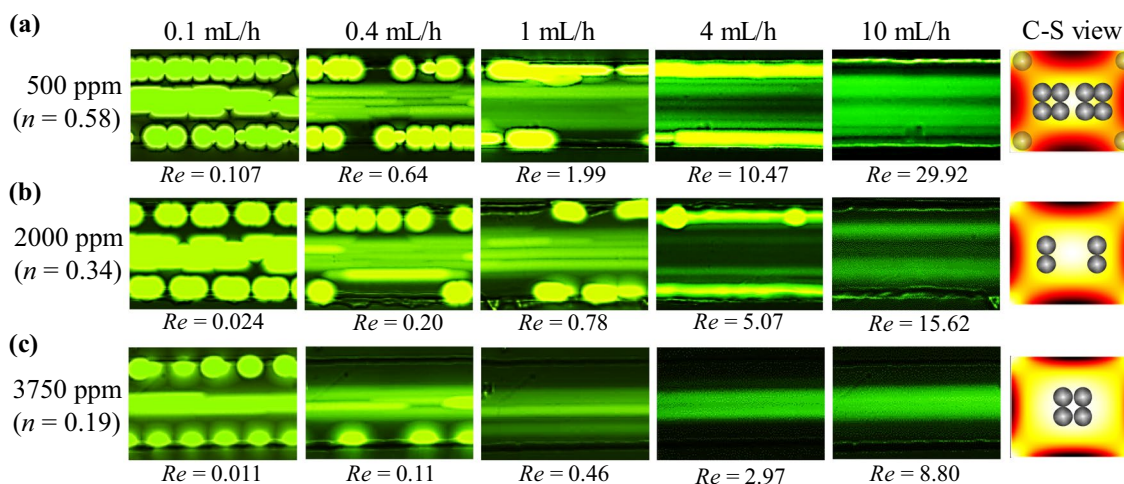
### 4.3 Effect of XG concentration

Figure 6 shows the motions of  $10 \mu\text{m}$  particles in the flow of 500 ppm, 2000 ppm and 3750 ppm XG solutions, respectively, through a  $54 \mu\text{m}$  deep microchannel

( $AR = 1.26$ ) in the same range of flow rates. Increasing the XG concentration enhances the fluid shear-thinning effect, which is reflected by the decreasing power-law index from  $n = 0.58$  to  $0.34$  and  $0.19$  (see Table 1). When the flow rate is less than  $1 \text{ mL/h}$ , the inertial effect is weak compared to the elastic effect such that particles travel near the channel center and corners in all three XG solutions. Increasing the flow rate enhances both the elastic and inertial lift forces, between which the latter increases at a greater rate because of its stronger dependence on fluid shear rate [see Eq. (2) vs. Equation (4)]. This leads to the observed shifting of  $10 \mu\text{m}$  particles towards an equilibrium mid-plane between the channel center and corners in 2000 ppm XG solution as noted above (see Fig. 6b). Reducing the XG concentration to 500 ppm decreases the elastic lift while increasing the inertial lift at the same flow rate because of the decrease in fluid viscosity (see Table 1) and in turn the increase in  $Re$ . It also changes the shear rate distribution (see the right-most schematic of Fig. 6a) and hence the flow-induced lift forces. The result is a significantly weakened two-stream focusing of particles near the channel center with a very small portion of them retained near the corners. In contrast, increasing the XG concentration to 3750 ppm enhances the elastic lift and decreases the inertial lift, yielding a single equilibrium particle position at the channel center (Fig. 6c). Figure 7 compares the particle intensity plots in the three XG solutions. With the increase of flow rate, particles are again observed to move away from the channel walls because of the enhanced inertial effect. Moreover, their equilibrium positions shift further towards the channel center when the XG concentration increases because of the enhanced elastic effect.



**Fig. 5** Scaled intensity plots for  $5 \mu\text{m}$ ,  $10 \mu\text{m}$  and  $20 \mu\text{m}$  particles in the flow of 2000 ppm XG solution through a  $54 \mu\text{m}$  deep microchannel at the flow rates of  $0.1 \text{ mL/h}$ ,  $1 \text{ mL/h}$  and  $10 \text{ mL/h}$ , respectively. The intensity values were obtained from the particle images in Fig. 4



**Fig. 6** Migration of 10  $\mu\text{m}$  particles in the flow of 500 ppm (with a power-law index of  $n = 0.58$ , **a**), 2000 ppm ( $n = 0.34$ , **b**) and 3750 ppm ( $n = 0.19$ , **c**) XG solutions through a 54  $\mu\text{m}$  deep straight rectangular microchannel under varying flow rates. The corresponding values of  $Re$  (strong function of XG concentration) are highlighted below the particle images (top view) at the channel outlet. The

schematics in the right-most column illustrate the equilibrium particle positions over the channel cross-section (C-S) (estimated from the images at 10 mL/h, drawn to scale), where the background color shows the contour of fluid shear rate (the darker the larger magnitude) in the corresponding XG solution

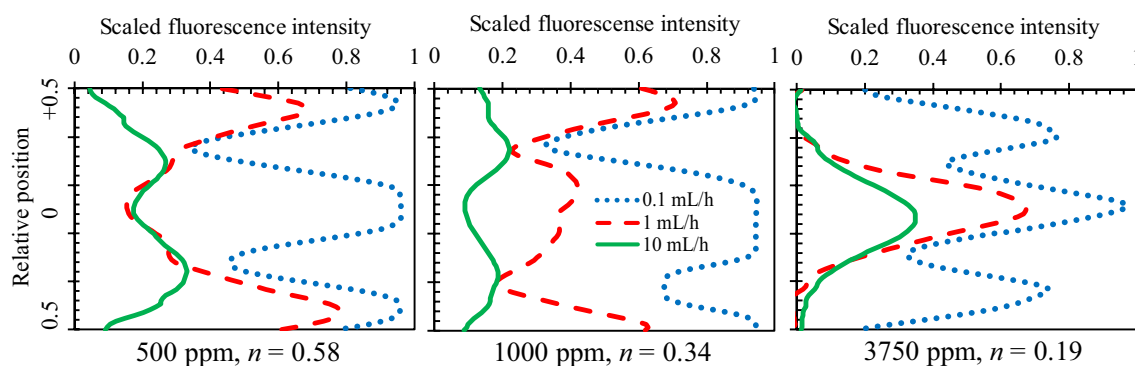


**Fig. 7** Scaled intensity plots for 10  $\mu\text{m}$  particles in the flow of 500 ppm, 2000 ppm and 3750 ppm XG solutions through a 54  $\mu\text{m}$  deep microchannel at the flow rates of 0.1 mL/h, 1 mL/h and 10 mL/h, respectively. The intensity values were obtained from the particle images in Fig. 6

## 5 Conclusions

We have conducted a systematic experimental study of the parametric effects on rigid particle motion in pseudoplastic XG solutions through straight rectangular microchannels. We find that when the flow rate is low, particles travel out of the channel near both the corners and centerline in all cases because of the sole action of elastic lift. With the increase of flow rate, nearly all the near-corner particles move away from the channel walls because of the enhanced wall-induced inertial lift. The only exception is the largest 20  $\mu\text{m}$  particles that stay near the corners in the entire range of flow rates under test because of the mutual actions of strong elastic lift and strong inertial lift.

Meanwhile, those near-centerline particles migrate outward because of the enhanced shear gradient-induced inertial lift unless the microchannel is too deep (127  $\mu\text{m}$  depth in our test, which expands the low shear rate region and reduces the elastic and inertial lift forces), or the particle is too small (5  $\mu\text{m}$  particles in our test, which experience an insufficient inertial lift), or the XG concentration is too high (3750 ppm in our test, which exhibits a strong elastic effect). Interestingly, these observed phenomena imply a potentially high throughout separation of rigid particles based on the difference in size in the flow of XG solutions through simple straight rectangular microchannels. We will study the feasibility of such a continuous sheath- and label-free particle separation in future work.



**Acknowledgements** This work was supported in part by NSF under Grant No. CBET-1704379.

## References

- Amini H, Lee W, Di Carlo D (2014) Inertial microfluidic physics. *Lab Chip* 14:2739–2761
- Asghari M, Serhatlioglu M, Ortaç B, Solmaz ME, Elbuken C (2017) Sheathless microflow cytometry using viscoelastic fluids. *Sci Rep* 7:12342. <https://doi.org/10.1038/s41598-017-12558-2>
- Asmolov ES (1999) The inertial lift on a spherical particle in a plane Poiseuille flow at large channel Reynolds number. *J Fluid Mech* 381:63–87
- Aytouna M, Paredes J, Shahidzadeh-Bonn N, Moulinet S, Wagner C, Amarouchene Y, Eggers J, Bonn D (2013) Drop formation in non-Newtonian fluids. *Phys Rev Lett* 110:034501
- Barnes HA, Hutton JF, Walters K (1989) An introduction to rheology. Elsevier, Amsterdam
- Bird RB, Armstrong RC, Hassager O (1987) Dynamics of polymeric liquids, Vol. 1. Wiley, New York
- Chen Q, Li D, Lin J, Wang MH, Xuan X (2017) Simultaneous washing and separation of nonmagnetic particles in an inertial ferrofluid/water co-flow. *Anal Chem* 89:6915–6920
- Connacher W, Zhang N, Huang A, Mei J, Zhang S, Gopesh T, Friend J (2018) Micro/nano acoustofluidics: materials, phenomena, design, devices, and applications. *Lab Chip* 18:1952–1996
- D’Avino G, Romeo G, Villone MM, Greco F, Netti PA, Maffettone PL (2012) Single line particle focusing induced by viscoelasticity of the suspending liquid: theory, experiments and simulations to design a micropipe flow-focuser. *Lab Chip* 12:1638–1645
- D’Avino G, Maffettone PL (2015) Particle dynamics in viscoelastic liquids. *J Non-Newton Fluid Mech* 215:80–104
- D’Avino G, Greco F, Maffettone PL (2017) Particle migration due to viscoelasticity of the suspending liquid and its relevance in microfluidic devices. *Annu Rev Fluid Mech* 49:341–360
- De Santo I, D’Avino G, Romeo G, Greco F, Maffettone PL (2014) Microfluidic Lagrangian trap for Brownian particles: three-dimensional focusing down to the nanoscale. *Phys Rev Appl* 2:064001
- Del Giudice F, Romeo G, D’Avino G, Greco F, Netti PA, Maffettone PL (2013) Particle alignment in a viscoelastic liquid flowing in a square-shaped microchannel. *Lab Chip* 13:4263–4271
- Del Giudice F, D’Avino G, Greco F, Netti PA, Maffettone PL (2015a) Effect of fluid rheology on particle migration in a square-shaped microchannel. *Microfluid Nanofluid* 19:95–104
- Del Giudice F, Madadi H, Villone MM, D’Avino G, Cusano AM, Vecchione R, Ventre M, Maffettone PL, Netti PA (2015b) Magnetophoresis ‘meets’ viscoelasticity: deterministic separation of magnetic particles in a modular microfluidic device. *Lab Chip* 15:1912–1922
- Del Giudice F, Sathish S, D’Avino G, Shen AQ (2017) “From the edge to the center”: viscoelastic migration of particles and cells in a strongly shear-thinning liquid flowing in a microchannel. *Anal Chem* 89:13146–13159
- Dhahir SA, Walters K (1989) On non-newtonian flow past a cylinder in a confined flow. *J Rheo* 33:781–804
- Di Carlo D (2009) Inertial microfluidics. *Lab Chip* 9:3038–3046
- Di Carlo D, Irimia D, Tompkins RG, Toner M (2007) Continuous inertial focusing, ordering, and separation of particles in microchannels. *Proc Natl Acad Sci* 104:18892–18897
- Di Carlo D, Edd JF, Humphry KJ, Stone HA, Toner M (2009) Particle segregation and dynamics in confined flows. *Phys Rev Lett* 102:094503
- Duffy DC, McDonald JC, Schueller OJA, Whitesides GM (1998) Rapid prototyping of microfluidic systems in Poly(dimethylsiloxane). *Anal Chem* 70:4974–4984
- Escudier MP, Smith S (1999) Turbulent flow of Newtonian and shear-thinning liquids through a sudden axisymmetric expansion. *Exp Fluid* 27:427–434
- Gauthier F, Goldsmith HL, Mason SG (1971a) Particle motions in non-Newtonian media. *Rheo Acta* 10:344–364
- Gauthier F, Goldsmith HL, Mason SG (1971b) Particle motions in non-newtonian media. II. Poiseuille flow. *Trans Soc Rheol* 15:297–330
- Geislinger TM, Franke T (2014) Hydrodynamic lift of vesicles and red blood cells in flow from Fåhræus & Lindqvist to microfluidic cell sorting. *Adv Colloid Interface Sci* 208:161–176
- Gou Y, Jia Y, Wang P, Sun C (2018) Progress of inertial microfluidics in principle and application. *Sensors* 18:1762
- Haase AS, Wood JA, Sprakel LM, Lammertink RG (2017) Inelastic non-Newtonian flow over heterogeneously slippery surfaces. *Phys Rev E* 95:023105
- Ho BP, Leal LG (1974) Inertial migration of rigid spheres in two-dimensional unidirectional flows. *J Fluid Mech* 65:365–400
- Ho BP, Leal LG (1976) Migration of rigid spheres in a two-dimensional unidirectional shear flow of a second-order fluid. *J Fluid Mech* 76:783–799
- Huang PY, Joseph DD (2000) Effects of shear thinning on migration of neutrally buoyant particles in pressure driven flow of Newtonian and viscoelastic fluids. *J Non-Newton Fluid Mech* 90:159–185
- Huang L, Bian S, Cheng Y, Shi G, Liu P, Ye X, Wang W (2017) Microfluidics cell sample preparation for analysis: advances in efficient cell enrichment and precise single cell capture. *Biomicrofluid* 11:011501
- Hur SC, Tse HTK, Di Carlo D (2010) Sheathless inertial cell ordering for extreme throughput flow cytometry. *Lab Chip* 10:274–280
- Japper-Jaafar A, Escudier MP, Poole RJ (2010) Laminar, transitional and turbulent annular flow of drag-reducing polymer solutions. *J Non-Newton Fluid Mech* 165:1357–1372
- Kang K, Lee SS, Hyun K, Lee SJ, Kim JM (2013) DNA-based highly tunable particle focuser. *Nat Commun* 4:2567
- Karimi A, Yazdi S, Ardekani AM (2013) Hydrodynamic mechanisms of cell and particle trapping in microfluidics. *Biomicrofluid* 7:021501
- Karnis A, Mason SG (1966) Particle motions in sheared suspensions. XIX. Viscoelastic media. *Tran Soc Rheol* 10:571–592
- Karnis A, Goldsmith HL, Mason SG (1963) Axial migration of particles in Poiseuille flow. *Nature* 200:159–160
- Kim B, Kim JM (2016) Elasto-inertial particle focusing under the viscoelastic flow of DNA solution in a square channel. *Biomicrofluid* 10:024111
- Kim MJ, Lee DJ, Youn JR, Song YS (2016) Two step label free particle separation in a microfluidic system using elasto-inertial focusing and magnetophoresis. *RSC Adv* 6:32090–32097
- Kung YC, Huang KW, Chong W, Chiou PY (2016) Tunnel dielectrophoresis for tunable, single-stream cell focusing in physiological buffers in high-speed microfluidic flows. *Small* 12:4343–4348
- Lapizco-Encinas BH (2018) On the recent developments of insulator-based dielectrophoresis: a review. *Electrophoresis*. <https://doi.org/10.1002/elps.201800285>
- Leal LG (1979) The motion of small particles in non-Newtonian fluids. *J Non-Newton Fluid Mech* 5:33–78
- Leal LG (1980) Particle motions in a viscous fluid. *Annu Rev Fluid Mech* 12:435–476
- Lee DJ, Brenner H, Youn JR, Song YS (2013) Multiplex particle focusing via hydrodynamic force in viscoelastic fluids. *Sci Rep* 3:3258
- Leshansky AM, Bransky A, Korin N, Dinnar U (2007) Tunable nonlinear viscoelastic “focusing” in a microfluidic device. *Phys Rev Lett* 98:234501

- Li D, Xuan X (2018) Fluid rheological effects on particle migration in a straight rectangular microchannel. *Microfluid Nanofluid* 22:49
- Li G, McKinley GH, Ardekani AM (2015) Dynamics of particle migration in channel flow of viscoelastic fluids. *J Fluid Mech* 785:486–505
- Li D, Lu X, Xuan X (2016) Viscoelastic separation of particles by size in straight rectangular microchannels: a parametric study for a refined understanding. *Anal Chem* 88:12303–12309
- Li D, Zielinski J, Kozubowski L, Xuan X (2018) Continuous sheath-free separation of drug-treated human fungal pathogen *Cryptococcus Neoformans* by morphology in biocompatible polymer solutions. *Electrophoresis* 39:2362–2369
- Liang L, Zhu J, Xuan X (2011) Three-dimensional diamagnetic particle deflection in ferrofluid microchannel flows. *Biomicrofluid* 5:034110
- Lim EJ, Ober TJ, Edd JF, Desai SP, Neal D, Bong KW, Doyle PS, McKinley GH, Toner M (2014a) Inertio-elastic focusing of bioparticles in microchannels at high throughput. *Nat Comm* 5:4120
- Lim H, Nam J, Shin S (2014b) Lateral migration of particles suspended in viscoelastic fluids in a microchannel flow. *Microfluid Nanofluid* 17:683–692
- Lindner A, Bonn D, Meunier J (2000) Viscous fingering in a shear-thinning fluid. *Phys Fluid* 12:256–261
- Liu C, Hu G (2017) High-throughput particle manipulation based on hydrodynamic effects in microchannels. *Micromachines* 8:73
- Liu C, Xue C, Chen X, Shan L, Tian Y, Hu G (2015) Size-based separation of particles and cells utilizing viscoelastic effects in straight microchannels. *Anal Chem* 87:6041–6048
- Liu C, Ding B, Xue C, Tian Y, Hu G, Sun J (2016) Sheathless focusing and separation of diverse nanoparticles in viscoelastic solutions with minimized shear thinning. *Anal Chem* 88:12547–12553
- Liu C, Guo J, Tian F, Yang N, Yan F, Ding Y, Wei J, Hu G, Nie G, Sun J (2017) Field-free isolation of exosomes from extracellular vesicles by microfluidic viscoelastic flows. *ACS Nano* 11:6968–6976
- Lu X, Xuan X (2015) Continuous microfluidic particle separation via elasto-inertial pinched flow fractionation. *Anal Chem* 87:6389–6396
- Lu X, Zhu L, Hua RM, Xuan X (2015) Continuous sheath-free separation of particles by shape in viscoelastic fluids. *Appl Phys Lett* 107:264102
- Lu X, Liu C, Hu G, Xuan X (2017) Particle manipulations in non-Newtonian microfluidics: a review. *J Colloid Interface Sci* 500:182–201
- Martel JM, Toner M (2014) Inertial focusing in microfluidics. *Annu Rev Biomed Eng* 16:371–396
- Mortazavi S, Tryggvason G (2000) A numerical study of the motion of drops in Poiseuille flow. Part 1. Lateral migration of one drop. *J Fluid Mech* 411:325–350
- Munaz A, Shiddiky MJA, Nguyen NT (2018) Recent advances and current challenges in magnetophoresis based micro magnetofluidics. *Biomicrofluid* 12:031501
- Nam J, Tan JK, Khoo BL, Namgung B, Leo HL, Lim CT, Kim S (2015) Hybrid capillary-inserted microfluidic device for sheathless particle focusing and separation in viscoelastic flow. *Biomicrofluid* 9:064117
- Nilsson J, Evander M, Hammarstrom B, Laurell T (2009) Review of cell and particle trapping in microfluidic systems. *Anal Chimica Acta* 649:141–157
- Novo P, Dell'Aica M, Janasek D, Zahedi RP (2016) High spatial and temporal resolution cell manipulation techniques in microchannels. *Analyst* 141:1888–1905
- Poole RJ, Escudier MP (2004) Turbulent flow of viscoelastic liquids through an axisymmetric sudden expansion. *J Non-Newton Fluid Mech* 117:25–46
- Rodd LE, Scott TP, Boger DV, Cooper-White JJ, McKinley GH (2005) The inertio-elastic planar entry flow of low-viscosity elastic fluids in micro-fabricated geometries. *J Non-Newton Fluid Mech* 129:1–22
- Romeo G, D'Avino G, Greco F, Netti PA, Maffettone PL (2013) Viscoelastic flow-focusing in microchannels: scaling properties of the particle radial distributions. *Lab Chip* 13:2802–2807
- Sajeesh P, Sen AK (2014) Particle separation and sorting in microfluidic devices: a review. *Microfluid Nanofluidics* 17:1–52
- Segre G, Silberberg A (1961) Radial particle displacements in Poiseuille flow of suspensions. *Nature* 189:209–210
- Seo KW, Byeon HJ, Huh HK, Lee SJ (2014a) Particle migration and single-line particle focusing in microscale pipe flow of viscoelastic fluids. *RSC Adv* 4:3512–3520
- Seo KW, Kang YJ, Lee SJ (2014b) Lateral migration and focusing of microspheres in a microchannel flow of viscoelastic fluids. *Phys Fluids* 26:063301
- Sibbitts J, Sellens KA, Jia S, Klasner SA, Culbertson CT (2018) Cellular analysis using microfluidics. *Anal Chem* 90:65–85
- Song HY, Lee SH, Salehiyan R, Hyun K (2016) Relationship between particle focusing and dimensionless numbers in elasto-inertial focusing. *Rheol Acta* 55:889–900
- Stoecklein D, Di Carlo D (2018) Nonlinear microfluidics. *Anal Chem*. <https://doi.org/10.1021/acs.analchem.8b05042>
- Takemura F, Magnaudet J, Dimitrakopoulos P (2009) Migration and deformation of bubbles rising in a wall-bounded shear flow at finite Reynolds number. *J Fluid Mech* 634:463–486
- Tian F, Cai L, Chang J, Li S, Liu C, Li T, Sun J (2018) Label-free isolation of rare tumor cells from untreated whole blood by interfacial viscoelastic microfluidics. *Lab Chip* 18:3436–3445
- Villone MM, D'Avino G, Hulsen MA, Greco F, Maffettone PL (2013) Particle motion in square channel flow of a viscoelastic liquid: migration vs. secondary flows. *J NonNewton Fluid Mech* 195:1–8
- Won D, Kim C (2004) Alignment and aggregation of spherical particles in viscoelastic fluid under shear flow. *J Non-Newton Fluid Mech* 117:141–146
- Xiang N, Dai Q, Ni Z (2016a) Multi-train elasto-inertial particle focusing in straight microfluidic channels. *Appl Phys Lett* 109:134101
- Xiang N, Zhang X, Dai Q, Cheng J, Chen K, Ni Z (2016b) Fundamentals of elasto-inertial particle focusing in curved microfluidic channels. *Lab Chip* 16:2626–2635
- Xiang N, Ni Z, Yi H (2018) Concentration-controlled particle focusing in spiral elasto-inertial microfluidic devices. *Electrophoresis* 39:417–424
- Xuan X, Zhu J, Church C (2010) Particle focusing in microfluidic devices. *Microfluid Nanofluid* 9:1–16
- Yan S, Zhang J, Yuan D, Li W (2017) Hybrid microfluidics combined with active and passive approaches for continuous cell separation. *Electrophoresis* 38:238–249
- Yang H, Gijs MAM (2018) Micro-optics for microfluidic analytical applications. *Chem Soc Rev* 47:1391–1458
- Yang S, Kim JY, Lee SJ, Lee SS, Kim JM (2011) Sheathless elasto-inertial particle focusing and continuous separation in a straight rectangular microchannel. *Lab Chip* 11:266–273
- Yang S, Lee SS, Ahn SW, Kang K, Shim W, Lee G, Hyun K, Kim JM (2012) Deformability-selective particle entrainment and separation in a rectangular microchannel using medium viscoelasticity. *Soft Matt* 8:5011–5019
- Yasuda K, Armstrong RC, Cohen RE (1981) Shear flow properties of concentrated solutions of linear and star branched polystyrenes. *Rheo Acta* 20:163–178
- Yuan D, Zhang J, Yan S, Pan C, Alici G, Nguyen NT, Li W (2015) Dean-flow-coupled elasto-inertial three-dimensional particle focusing under viscoelastic flow in a straight channel with asymmetrical expansion–contraction cavity arrays. *Biomicrofluid* 9:044108

- Yuan D, Zhang J, Yan S, Peng G, Zhao Q, Alici G, Du H, Li W (2016) Investigation of particle lateral migration in sample-sheath flow of viscoelastic fluid and Newtonian fluid. *Electrophoresis* 37:2147–2155
- Yuan D, Zhao Q, Yan S, Tang SY, Alici G, Zhang J, Li W (2018) Recent progress of particle migration in viscoelastic fluids. *Lab Chip* 18:551–567
- Zhang J, Yan S, Yuan D, Alici G, Nguyen NT, Warkiani ME, Li W (2016a) Fundamentals and applications of inertial microfluidics: a review. *Lab Chip* 16:10–34
- Zhang J, Yan S, Yuan D, Zhao Q, Tan SH, Nguyen NT, Li W (2016b) A novel viscoelastic-based ferrofluid for continuous sheathless microfluidic separation of nonmagnetic microparticles. *Lab Chip* 16:3947–3956
- Zhou Y, Song L, Yu L, Xuan X (2017) Inertially focused diamagnetic particle separation in ferrofluids. *Microfluid Nanofluid* 21:14

**Publisher's Note** Springer Nature remains neutral with regard to jurisdictional claims in published maps and institutional affiliations.